

Massive-training Artificial Neural Network Coupled with Dimensionality Reduction for Computer-aided Detection of Polyps in CT Colonography

Jun Zhang¹, Kenji Suzuki¹

1. Department of Radiology, The University of Chicago, 5841 South Maryland Avenue,
Chicago, Illinois 60637

Send Correspondence To:

Jun Zhang

Department of Radiology, The University of Chicago

5841 South Maryland Avenue, MC 2026

Chicago, IL 60637

E-mail: junzhang@uchicago.edu

Phone: (312) 823-7619

Fax: (773) 702-0371

Abstract

A major challenge in the current computer-aided detection (CAD) of polyps in CT colonography (CTC) is to reduce the number of false positive (FP) detections while maintaining a high sensitivity level. A pattern-recognition technique based on the use of an artificial neural network (ANN) as a filter, which is called a massive-training ANN (MTANN), has been developed recently for this purpose. The MTANN is trained with a massive number of subvolumes extracted from input volumes together with the teaching volumes containing the distribution for the “likelihood of being a polyp”, hence the term “massive training”. Because of the large number of subvolumes and the high dimensionality of voxels in each input subvolume, the training of an MTANN is time-consuming. In order to solve this time issue and make an MTANN work more efficiently, we propose here a dimension reduction method for an MTANN by using Laplacian eigenfunctions (LAPs), denoted as a LAP-MTANN. Instead of input voxels, the LAP-MTANN uses the dependence structures of input voxels to compute the selected LAPs of the input voxels from each input subvolume and thus reduces the dimension of the input vector to the MTANN. Our database consisted of 200 CTC datasets obtained from 100 patients, each of whom was scanned in both supine and prone positions. Fourteen patients had 26 polyps, 12 of which were 5-9 mm and 14 were 10-25 mm in size. To investigate the basic properties of a LAP-MTANN, we trained the LAP-MTANN with actual polyps and a single source of FPs, which were rectal tubes. We applied the trained LAP-MTANN to simulated polyps and rectal tubes. The results showed that the performance of LAP-MTANNs with 20 LAPs was advantageous to that of the original MTANN with 171 inputs. To test the feasibility of the LAP-MTANN, we compared the LAP-MTANN with the original MTANN in the distinction between actual polyps and various types of FPs. The original MTANN yielded a 96% (25/26) by-polyp sensitivity at an FP rate of 3.2 (315/100) per patient, whereas the LAP-MTANN achieved a comparable performance, i.e., an FP rate of 2.9 (289/100) per patient at the same sensitivity level. With the use of the dimension reduction architecture, the time required for training was reduced from 38 hours to four

hours. The classification performance in terms of area under the receiver-operating-characteristic curve of the LAP-MTANN (0.88) was higher than that of the original MTANN (0.84), at a statistically significant level (P-value=0.003).

I. Introduction

Colorectal cancer is the second leading cause of cancer death in the United States. Early detection and removal of polyps (the precursors of colorectal cancers) is a promising strategy for enhancing patients' chance of survival. CT colonography (CTC) is an emerging technique for mass screening of colorectal carcinoma. The diagnostic performance of CTC in detecting polyps, however, remains uncertain because of a propensity for perceptual errors and substantial variations among readers in different studies. Computer-aided detection (CAD) of polyps has the potential to overcome these difficulties with CTC. CAD provides for radiologists the locations of suspicious polyps for their review, thus improving the diagnostic performance in the detection of polyps.

Applying CAD schemes for detection of polyps is a very challenging task, because the polyps can have various sizes and shapes. Furthermore, there are numerous colon folds and residual leftover colonic materials on the colon wall that mimic polyps. A number of researchers have recently developed automated or semi-automated CAD schemes in CTC. Although the performance of current CAD schemes has demonstrated a great potential, some limitations remain. One of the major limitations is a relatively large number of false-positive (FP) detections, which is likely to confound the radiologist's image interpretation task and thus lower their efficiency. A large number of FPs could adversely affect the clinical application of CAD for colorectal cancer screening. Therefore, methods for removal of computer FPs are demanded strongly.

The common sources of FPs are haustral folds, residual stool, rectal tubes, and extra-colonic structures such as the small bowel and stomach, as reported in Ref [?]. Various methods have been proposed for the reduction of FPs, with variable success. Summers et al. [?, ?] employed the geometrical features on the inner surface of colon wall, such as the mean, Gaussian, and principal curvatures, etc., to find polyp candidates. Yoshida et al. [?] and Nappi et al. [?] further characterized the curvature measures by using a shape index and curvedness to distinguish polyp candidates from the normal tissues of colon wall. Paik

et al. [?] and Kiss et al. [?] presented another solution for polyp detection in which they utilized the normal (rather than the curvature) and sphere fitting as references to extract some geometric features on the polyp surfaces. Because these traditional surface shape-based descriptions are sensitive to the irregularity of the colon wall, these CAD methods share a relatively high FP rate. Gokturk et al. [?] developed a scheme based on statistical pattern recognition, and they applied a 3D-pattern processing method to the reduction of FPs. Acar et al. [?] used edge-displacement fields to model the changes in consecutive cross-sectional views of CTC data, as well as quadratic discriminant analysis. Jerebko et al. [?, ?] used a standard ANN to classify polyp candidates and improved the performance by incorporating a committee of ANNs and a committee of support vector machines. Yao et al. [?] explored image segmentation methods to reduce FPs. Iordanescu and Summers [?] developed an image-segmentation-based approach for the reduction of FPs due to rectal tubes.

The performance of a CAD scheme usually involves a trade-off between sensitivity and specificity. It is important to remove as many types of FPs as possible, while the sensitivity of a CAD scheme is maintained. For addressing this issue, a three-dimensional (3D) massive-training artificial neural network (MTANN) and a mixture of expert 3D MTANNs were developed for elimination of a single type of FP [?] and multiple types of FPs [?], respectively. The mixture of expert 3D MTANNs consists of several expert 3D MTANNs in parallel, each of which is trained independently by use of a specific type of non-polyp and a common set of various types of polyps. Each expert MTANN acts as an expert for distinguishing polyps from a specific type of non-polyp. It was demonstrated in Ref. [?] that this mixture of expert MTANNs was able to eliminate various types of FPs at a high sensitivity level.

The training of an MTANN is, however, very time-consuming [?, ?, ?, ?, ?, ?, ?]. For example, the training of a 3D MTANN with ten polyps and ten FPs may take 38 hours on a PC-based workstation [?, ?]. The training time will increase when the number of training cases increases. To address this time issue and make an MTANN work more efficiently, we propose here a dimension-reduction-based MTANN. In the MTANN scheme, the features are

the large number of neighboring voxel values selected from each subvolume and thus they have some underlying geometric structures and are highly dependent. Motivated by this fact, we employ a manifold -based dimension reduction technique, Laplacian eigenfunction[?], to improve the efficiency of the original MTANN. This will be demonstrated by use of both simulation and actual clinical data. Other nonlinear dimension reduction techniques such as the diffusion map[?] and IsoMap[?] would have comparable results since they can take the local geometry information fairly well. While the classical principal component analysis is known for being sensitive to outliers and cannot incorporate the local intrinsic structure.

The paper is organized as follows: In section 2, we first describe our CTC database and review the basics of an MTANN, and we then explain the technical details for the improvement by using Laplacian eigenfunctions. In section 3, we compare the results by applying an MTANN with and without LAPs in experiments with both simulated and actual polyps. Finally, we further discuss the statistical issues of employment of LAPs in section 4 and give a conclusion in section 5.

II. Materials and Methods

A. Database

The database used in this study consisted of 200 CTC datasets obtained from 100 patients acquired at the University of Chicago Medical Center. Each patient was scanned in both supine and prone positions. Each reconstructed CT section had a matrix size of 512×512 pixels, with an in-plane pixel size of 0.5–0.7 mm. In this study, we used 5 mm as the lower limit on the size of polyps. Fourteen patients had 26 colonoscopy-confirmed polyps, 12 of which were 5-9 mm and 14 were 10-25 mm in size. We applied our initial CAD scheme for detection of polyps in CTC to our CTC database. Our initial polyp-detection scheme is a standard CAD approach which consists of 1) colon segmentation based on CT value-based analysis and colon tracing, 2) detection of polyp candidates based on morphological analysis

on the segmented colon, 3) calculation of 3D pattern features of the polyp candidates [?], and 4) quadratic discriminant analysis for classification of the polyp candidates as polyps or non-polyps based on the pattern features. Our initial CAD scheme yielded 96% (25/26) by-polyp sensitivity with 4.9 (489/100) FPs per patient. Forty-six true-positive polyp detections in both supine and prone CTC volumes constituted 26 polyps. The major sources of FPs included rectal tubes, stool, haustral folds, colonic walls, and the ileocecal valve. These CAD detections were used for experiments for evaluating the performance of 3D MTANNs.

B. Basics of an MTANN

A 2D MTANN was originally developed for distinguishing a specific opacity from other opacities [?]. The 2D MTANN was applied to the reduction of FPs in computerized detection of lung nodules in chest radiography [?], low-dose CT [?, ?], and the suppression of ribs in chest radiographs [?]. A 3D MTANN was recently developed for processing 3D volume data in CTC [?, ?]. The architecture of a 3D MTANN is shown in Fig.1. A 3D MTANN consists of a linear-output multilayer ANN model for regression, which is capable of operating on voxel data directly [?, ?]. The 3D MTANN is trained with input CTC volumes and the corresponding teaching volumes for enhancement of polyps and suppression of non-polyps. The input to the expert 3D MTANN consists of a collection of voxel values in a subvolume, V_s , extracted from an input volume, denoted as a vector $I = (I^1, \dots, I^n) \in \mathbb{R}^n$, where each I^i denotes one input voxel in V_s . Here, n is the number of voxels in a subvolume of a fixed size. The output of an MTANN is a continuous scalar value, which is associated with the center voxel in the subvolume. The output is denoted by

$$O(x, y, z) = NN\{I(x - p, y - q, z - r) | (p, q, r) \in V_s\}.$$

The teaching volume for polyps contains a 3D Gaussian distribution with standard deviation σ_T , which approximates the average shape of polyps, and that for non-polyps contains only

zeros. This distribution represents the likelihood of being a polyp:

$$T(x, y, z) = \begin{cases} \frac{1}{\sqrt{2\pi}\sigma_T} e^{-\frac{x^2+y^2+z^2}{2\sigma_T^2}}, & \text{for a polyp} \\ 0, & \text{for non-polyps.} \end{cases}$$

To enrich the training samples, a massive number of overlapping subvolumes are extracted from a training volume V_T , and the same number of single voxels are extracted from the corresponding teaching volume as teaching values. The error to be minimized in training is given by

$$E = \frac{1}{P} \sum_i \sum_{(x,y,z) \in V_T} (T_i(x, y, z) - O_i(x, y, z))^2,$$

where i is a training case number, O_i is the output of the MTANN for the i^{th} case, T_i is the teaching value for the i^{th} case, and P is the total number of training voxels in the training volume. The MTANN is trained by a linear-output back-propagation algorithm[?, ?].

[Figure 1 about here.]

After training, the MTANN is expected to output the highest value when a polyp is located at the center of the subvolume, a lower value as the distance from the subvolume center increases, and approximately zero when the input subvolume contains a non-polyp. The entire output volume is obtained by scanning of the whole input CTC volume to the MTANN. For the distinction between polyps and non-polyps, a 3D scoring method based on the output volume of the trained MTANN is applied. A score for a polyp candidate is defined as

$$S = \sum_{(x,y,z) \in V_E} f_G(x, y, z; \sigma) \times O(x, y, z),$$

where

$$f_G(x, y, z; \sigma) = \frac{1}{\sqrt{2\pi}\sigma} e^{-\frac{x^2+y^2+z^2}{2\sigma^2}}.$$

is a 3D Gaussian weighting function with standard deviation σ with its center corresponding to the center of the volume for evaluation, V_E ; V_E is the volume for evaluation, which

is sufficiently large to cover a polyp or a non-polyp; and $O(x, y, z)$ is the output of the trained MTANN. The score is the weighted sum of the estimates of the likelihood that a polyp candidate volume contains an actual polyp near the center, that is, a high score would indicate a polyp and a low score would indicate a non-polyp. The same 3D Gaussian weighting function is used as in the teaching volumes. Threshold is then performed on the scores for the distinction purpose.

[Figure 2 about here.]

C. LAP-MTANN: A 3D MTANN based on manifold embedding using Laplacian eigenfunctions

One drawback of the MTANN proposed above is that the selected patterns are regarded as independent inputs to the ANN and the correlation among close sampled patterns are ignored. In our situation, the training patterns sampled from common candidate volumes are highly overlapped, and thus the corresponding voxel values are strongly dependent on each other. This intrinsic dependence structure of the selected patterns should be incorporated in the MTANN scheme.

Another drawback of an MTANN is that the training is very time-consuming. This is caused by the high dimensionality of the input vector to the linear-output ANN and the large number of training subvolumes extracted from training volumes. The use of a smaller subvolume can reduce the dimensionality of the input layer. However, the input subvolume to an MTANN has to be large enough to cover a sufficient part of a polyp candidate. A practical choice of a sphere-shaped subvolume gives $n = 171$ (see Fig. 2). This also limits the application of an MTANN to polyp candidates of large size. For reducing the training time, one possibility is to reduce the number of training subvolumes. The reduction of the number of training patterns, however, will obviously lead to an insufficiently trained MTANN and directly make the MTANN lose the power to distinguish polyps from non-polyps. Naturally,

this leads us to another way of reducing of the dimensionality of the input layer.

Motivated from the above observation, we propose using Laplacian eigenfunctions to embed the input subvolume patterns, without abuse of notation denoted as $I \in \mathbb{R}^n$, into a lower dimensional manifold \mathcal{M} and then applying ANN to the embedded patterns $C \in \mathbb{R}^d$, where $d \ll n$. The method not only incorporates the correlation among inputs, but also achieves the dimension reduction of inputs. This implementation procedure is stated below:

Step 1. Normalization of Data. We first normalize the inputs $\{I_i = (I_i^1, \dots, I_i^n) : i = 1, \dots, N\}$ by subtracting the sample mean $\mu = (\mu^1, \dots, \mu^n)$, where $\mu^j = \frac{1}{N} \sum_{i=1}^N I_i^j$, for $j = 1, \dots, n$ and then dividing by the estimated standard deviation $\sigma^j = \sqrt{\frac{1}{N} \sum_{i=1}^N (I_i^j - \mu^j)^2}$. We will use B to denote the normalized data. For a comprehensive exploration of PCs, we refer readers to a book by Anderson [?].

Step 2. Construction of an adjacency graph. Following above, we let $r_{ij} = \sum_{k=1}^n B_i^k B_j^k$ denote the correlation coefficient between B_i and $B_j, i, j = 1, \dots, N$. Now let G denote a graph with N nodes. The i^{th} node corresponds to the i^{th} input $B_i = (B_i^1, \dots, B_i^n)$. We connect nodes i to j with an edge if $r_{ij} < \epsilon$ for some specified constant $\epsilon > 0$. That is, an edge is put only for close ϵ -neighbors. This implementation reflects the general phenomena that faraway nodes are usually less important than close neighbors.

Step 3. Assigning of a weight matrix. For each connected edge between nodes i and j , we assign the weight

$$W_{ij} = e^{-\frac{\|B_i - B_j\|^2}{t}}$$

where t is a suitable constant and $t=1.0$ in our computation. Otherwise, we assign $W_{ij} = 0$. Thus, W is a symmetric matrix. The weight matrix W approximates the manifold structure of the inputs $\{I_i : i = 1, \dots, N\}$ in an intrinsic way. In other words, it models the geometry of inputs by preserving the local structure. The chosen Gaussian weight relates to heat kernel and the justification can be found in reference[20].

Step 4. Laplacian eigenfunctions and embedding map. Let D be a diagonal matrix whose entries are the row or column sums of W , $D_{ii} = \sum_j W_{ji}$. And let $L = D - W$

be the associated Laplacian matrix. Next compute the eigenvectors and eigenvalues for the generalized eigenvector problem:

$$BLB^T \mathbf{v} = \lambda BDB^T \mathbf{v}.$$

Let $\mathbf{v}_0, \dots, \mathbf{v}_{m-1}$ be the eigenvectors, ordered according to their eigenvalues, $\lambda_0 < \lambda_1 < \dots < \lambda_{m-1}$. Let the $m \times K$ size transformation matrix to be

$$W_{lap} = (\mathbf{v}_0, \mathbf{v}_1, \dots, \mathbf{v}_{K-1}).$$

Thus, the embedding is as follows: $B_i \longrightarrow C_i = W_{lap}^T B_i$, where C_i is a K -dimensional vector. The overall embedding map is given as $I_i \longrightarrow C_i = W_{lap}^T I_i$.

D. Simulation Experiments

To understand the basic properties of a LAP-MTANN for FP reduction, we carried out an experiment with simulated polyps and rectal tubes, which are one of the major sources of FPs. A polyp is modeled as a sphere with diameter d , and a rectal tube is modeled as a hollow cylinder with diameter d_T , length ln , and wall thickness t_w . We employed these simple models with the aim of understanding the essential role of a LAP-MTANN. We trained a LAP-MTANN with ten actual polyps and ten rectal tubes (see the top part of Fig. 3). We did this because this simplified simulated phantom could reveal the fundamental mechanism of the proposed approaches. The simulated CTC volumes with polyps and rectal tubes of five different sizes (d : 6, 8, 10, 12, 15, and 25 mm; d_T : 10, 12, 14, 15, and 16 mm) are illustrated in the top part of Fig. 4. According to the measurements of actual polyps and rectal tubes in clinical CTC volumes, the CT values for the simulated polyps and rectal tubes were set to 60 and 180, respectively. The length ln was 70 mm and the wall thickness t_w was 2 mm.

[Figure 3 about here.]

[Figure 4 about here.]

Experiments with Actual CTC Data

To evaluate and compare our proposed 3D LAP-MTANNs with original 3D MTANNs, we carried out experiments with actual polyps and non-polyps in our CTC database.

Ten representative polyp volumes (the same actual polyps as above for simulation) from 46 true-positive volumes in our CTC database and ten various non-polyp volumes from another database were manually selected as the training cases for a 3D MTANN (see Fig. 4). The selection was based on the visual appearance of polyps and non-polyps in terms of size, shape and contrast to represent the database. A three-layer structure was employed for the 3D MTANN, because it has been shown theoretically that any continuous mapping can be approximated by a three-layer ANN. Based on our previous studies [?, ?], the size of the training volume and the standard deviation of the 3D Gaussian distribution were selected to be $15 \times 15 \times 15$ voxels and 4.5 voxels, respectively. A quasisphere cubic subvolume of kernel size $7 \times 7 \times 7$ containing $2 \times (9 + 21) + 3 \times 37 = 171$ voxels was employed as the input subvolume for a 3D MTANN, as shown in Fig 2 above. Thus, the input layer of the original MTANN has 171 units. The training subvolumes were sampled every other voxel in each dimension; thus, the total number of training subvolumes for both TPs and FPs were $8 \times 8 \times 8 \times 20 = 10,240$. This sampling scheme also explains the strong dependence structure among the closely sampled patterns which are measured by correlation coefficient r_{ij} for the i^{th} and j^{th} patterns, see section 2.3 for details. The number of hidden units was determined to be 25 by an algorithm for designing the structure of an ANN [?].

[Figure 5 about here.]

[Figure 6 about here.]

[Figure 7 about here.]

We used receiver-operating-characteristic (ROC) analysis [?] to assess the performance of the original MTANN and the LAP-MTANN in the task of distinguishing polyps from non-polyps. The area under the maximum-likelihood-estimated binormal ROC curve (AUC) was used as an index of performance. We used ROCKIT software (version 1.1b, available at http://xray.bsd.uchicago.edu/kr1/KRL_ROC/software_index6.htm) to determine the p value of the difference between two AUC values [?]. For the evaluation of the overall performance of a CAD scheme with 3D PC-MTANNs, free-response ROC (FROC) analysis was used [?].

III. Results

A. Simulation Experiments

The actual training rectal tubes and their output volumes of the trained 3D LAP-MTANN with 20 LAPs and the trained original 3D MTANN are comparable and illustrated in the lower part of Fig. 3. Both output volumes are well suppressed around the rectal-tube locations. The simulated polyps and rectal tubes and their output are illustrated in Fig 4. Polyps are represented by bright voxels, whereas rectal tubes appear mostly dark with some bright segments around them. Overall, the LAP-MTANN performs slightly better than MTANN, see Fig 6 for the illustration on polyps and non-polyps. The LAP-MTANN performs better than the original MTANN for some polyps and non-polyps, while the original MTANN does better for several cases, as seen in Fig 7 for selected ROIs for illustration. The scores of the 3D LAP-MTANN and the original 3D MTANN for various sized simulated polyps and rectal tubes are shown in Fig. 8. The original 3D MTANN scores for polyps smaller than 4.5 mm overlap with those of rectal tubes, indicating that simulated polyps larger than 4.5 mm could be distinguished from rectal tubes. On the other hand, although the difference between the 3D LAP-MTANN scores for polyps larger than 11 mm and for rectal tubes becomes smaller, there is no overlap between the curves for polyps and rectal

tubes. This result indicates that the performance of the 3D LAP-MTANN can be superior to that of the original 3D MTANN for distinction of polyps from rectal tubes.

[Figure 8 about here.]

[Figure 9 about here.]

To investigate the effect of different numbers of LAPs used, we plotted the scores of the LAP-MTANNs with various numbers of LAPs for simulated polyps and rectal tubes in Fig 8. When the number of LAPs increases from 20 to 100, the scores vary slightly but have the same trend. The maximum scores for rectal tubes are well separated from the minimum scores for polyps. This adds evidence that the classification performance of the LAP-MTANNs with different numbers of LAPs is approximately at the same level. To investigate the effect of different scanning kernel sizes of subvolumes on the performance of a LAP-MTANN, we trained the LAP-MTANN with a larger kernel size of $9 \times 9 \times 9$ voxels (437 voxels in each spherical subvolume). We used top 20 LAPs for this larger-kernel LAP-MTANN. The training time for this LAP-MTANN was about 4 hours, which was same as that with a kernel size of $7 \times 7 \times 7$ voxels, because the numbers of LAPs and training subvolumes were the same. It turns out the scores for simulated polyps and rectal tubes drop almost uniformly from a kernel size of 7 to that of 9. And there is no obvious advantage to employing large kernels in this case.

B. Training

We trained an original 3D MTANN with the parameters described in the previous section. The training with 500,000 iterations took 38 hours, and the mean absolute error between teaching and output values converged approximately to 0.091. To compare with the proposed LAP-MTANN, we used all of the same above data and parameters with 20 top LAPs (i.e., $n = 20$). Certainly, different numbers of top LAPs selected would change the result slightly, but the difference was not statistically significant in our studies. We will further justify our

choice of n below. The training of a LAP-MTANN was performed with 500,000 iterations, and the mean absolute error converged approximately to 0.10. The training time was reduced substantially to 4 hours.

C. Evaluation of the performance of LAP-MTANNs

Table 1 shows the effect of various numbers of top LAPs on the performance of LAP-MTANNs in the distinction between actual polyps and non-polyps. The AUC values of the 3D LAP-MTANNs with various numbers of LAPs were statistically significantly different from that of the original 3D MTANN. The ROC curve of the 3D LAP-MTANN with 20 LAPs is plotted in Fig. 10 together with that of the original MTANN. Figure. 11 shows FROC curves indicating the overall performance of the original 3D MTANN and the 3D LAP-MTANN for FP reduction. The original MTANN was able to eliminate 36% (174/489) of FPs without removal of any of 46 true positives, i.e., a 96%(25/26) overall by-polyp sensitivity was achieved at an FP rate of 3.15 (315/100) per patient. The LAP-MTANN achieved a slightly better performance: it eliminated 43% (211/489) of FPs without removal of any true positives. Among them, 160 FPs overlapped with those removed by the original MTANN (95%). The LAP-MTANN did not remove ten FPs which the original MTANN removed, but removed 47 other FPs.

[Table 1 about here.]

[Figure 10 about here.]

[Figure 11 about here.]

IV. Discussion

In the scheme of MTANN, the input patterns consist of a large number (171 in this study) of neighboring voxel values. A lot of these voxels are redundant and may contain much

noise in the dataset. On the one hand, large volumes of patterns require long time for training; and on the other hand, it can make the classification task more difficult because of curse of dimensionality. The reduction of the training time is necessary for practical clinical applications. Dimension reduction can considerably reduce the training time and improve the performance of an MTANN significantly. In our proposed procedure, we first apply the classical principal component (PC) analysis to eliminate noise in the data. The PCs of input voxels are the linear combinations of voxels which preserve the variations in the data. The variations of the PCs of the voxel values can approximate the variations of the underlying features. However, the patterns actually overlap with close-by patterns. The more they overlap, the higher they depend on each other. These close patterns usually have some intrinsic manifold structures and this information can be employed to more accurately embed the patterns in a lower dimensional space. Laplacian eigenfunctions is a well-known manifold learning technique for dimension reduction. It constructs a graph by regarding each pattern as a node and then compute the graph Laplacian eigenfunctions. In our proposed scheme, we measure the dependence of patterns by correlation coefficients and map the close-by patterns to close-by points in the reduced lower dimensional space via the Laplacian eigenfunctions. See Fig 12 below, for an illustration on a subset of 512 training patterns selected from a polyp. One can observe that the top Laplacian functions can learn the intrinsic dependence structures and map close ones to their clusters while the classical PCs just spread the patterns out. Thus the Laplacian approach fits the MTANN scheme very well. We note that other closely related manifold based dimension technique has also been employed in CAD such as in [?] Summers etc. have applied a diffusion map for feature selection purposes, which is different from our usage.

Practically one trains each specific LAP-MTANN for each specific type of false positive beforehand and then applies trained LAP-MTANNs to process CTC cases. Note that the processing time of new CTC cases has also been reduced to about one tenth of the original MTANN processing time, less than 2 minutes per patient based on our database. Neverthe-

less, the CTC diagnosis is not necessarily real-time. The accuracy in terms of AUC value has also improved from 0.84% to 0.88%. We expect that further higher improvement can be obtained in practice, since multiple LAP-MTANNs would be applied with each trained for specific task.

[Figure 12 about here.]

One limitation of the study is the use of a limited number of cases with polyps. Evaluation using a larger database will generally give more reliable results on the performance of a LAP-MTANN. However, it should be noted that, though the 3D LAP-MTANN trained with only 10 polyps, the performance for 27 polyps including the 10 polyps and 17 non-training polyps were very similar at a high sensitivity level. This observation indicates the robustness of the 3D LAP-MTANN. Thus, we expect that the performance of the 3D LAP-MTANN on a larger database would be potentially comparable to that demonstrated in this study.

V. Conclusion

We have developed 3D LAP-MTANNs with the aim of improving the efficiency of an MTANN. With Laplacian eigenfunctions, we were able to reduce the time required for training of MTANNs substantially while the classification performance was maintained in terms of the reduction of FPs in a CAD scheme for detection of polyps in CTC.

List of Figures

1	Architecture of a LAP-MTANN consisting of a massive-subvolume training scheme, dimension reduction by Laplacian eigenfunctions, and a linear-output ANN model. The input CTC volumes including a polyp or a non-polyp are divided voxel by voxel into a large number of overlapping 3D subvolumes. Instead of all voxel values in each subvolume, only the top n Laplacian eigenfunctions of them are entered as an input vector to the linear-output ANN.	20
2	Dimensionality reduction of the scanning spherical input subvolume to the linear-output ANN via Laplacian eigenfunctions. Each square matrix represents a cross section at a certain z position in the input subvolume, where z_0 represents the central slice of the subvolume. A gray square in each section indicates the input voxel to the linear-output ANN, and a white square indicates an unused voxel. The 171 dimensional original input vector is converted to the LAPs vector. The top n LAPs are extracted and entered to the linear-output ANN.	21
3	Illustrations of training (a) polyps and the corresponding output volumes of the trained original 3D MTANN and 3D LAP-MTANNs with top 20 eigenfunctions and (b) rectal tubes and the corresponding output volumes of the original 3D MTANN and 3D LAP-MTANNs in a resubstitution test. Shown are the central axial slices of 3D volumes. Training volumes for polyps contain 3D Gaussian distributions at the center, whereas those for non-polyps are completely dark, i.e., the voxel values for non-polyps are zero. In the output volumes of the original 3D MTANN and the 3D LAP-MTANNs, polyps are represented by bright voxels, whereas non-polyps are dark.	22
4	Illustrations of simulated polyps and rectal tubes and the corresponding output volumes of the original 3D MTANN and the LAP-MTANN with 20 eigenfunctions.	23
5	Illustrations of training non-polyps and the corresponding output volumes. The true polyps used for training are the same as for the simulation. The central axial slices of the 3D volumes are shown.	24
6	Illustrations of the performance of the trained 3D original and LAP-MTANNs with top 20 eigenfunctions on polyps and non-polyps, and the corresponding output volumes. The central axial slices of the 3D volumes are shown. The performance of the LAP-MTANN is comparable to that of the original MTANN.	25
7	Illustrations of selected non-polyps, where the LAP-MTANN works better than the original MTANN on the first three and the original MTANN works better than the LAP-MTANN on the last two. The central axial slices of the 3D volumes are shown.	26
8	Effect of the size of simulated polyps on distinction between simulated polyps and rectal tubes based on LAP-MTANN and MTANN scores. Based on the scores, polyps larger than 4.5 mm can be distinguished from rectal tubes by the original 3D MTANN, whereas polyps of all sizes can be distinguished from rectal tubes by the 3D LAP-MTANN with 20 eigenfunctions.	27

9	LAP-MTANN scores with various numbers of selected top Laplacian eigenfunctions in distinction between simulated polyps and rectal tubes.	28
10	Comparison between the performance of the LAP-MTANN with 20 Laplacian eigenfunctions and that of the original MTANN. The difference between the AUC values for the ROC curves was not statistically significant ($p = 0.003$).	29
11	FROC curves indicating the performance of the LAP-MTANN with 20 Laplacian eigenfunctions and that of the original MTANN.	30
12	The top two PCs and Laplacian eigenfunctions of a set of 512 training patterns.	31

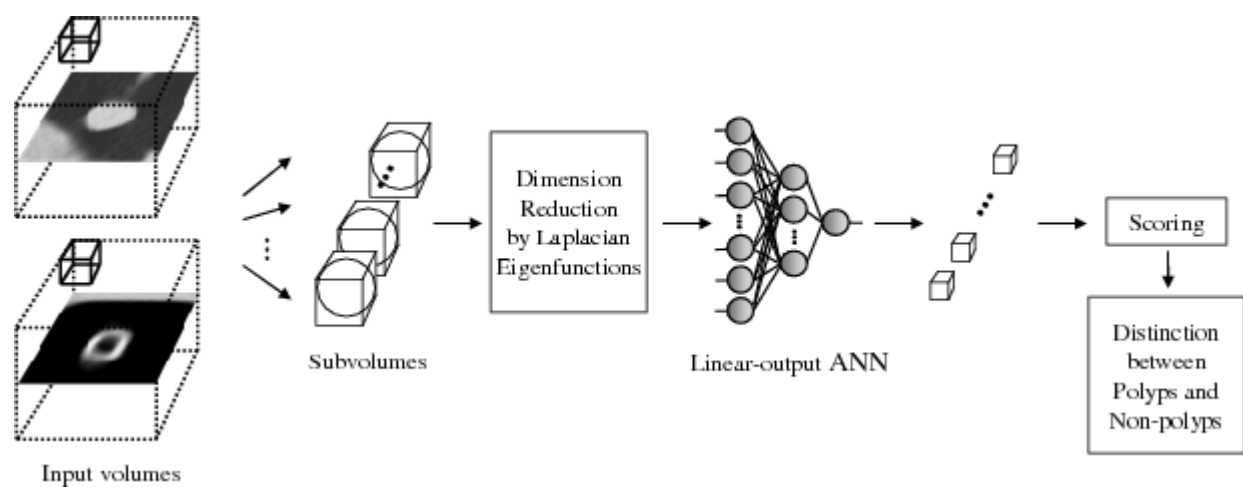


Figure 1: Architecture of a LAP-MTANN consisting of a massive-subvolume training scheme, dimension reduction by Laplacian eigenfunctions, and a linear-output ANN model. The input CTC volumes including a polyp or a non-polyp are divided voxel by voxel into a large number of overlapping 3D subvolumes. Instead of all voxel values in each subvolume, only the top n Laplacian eigenfunctions of them are entered as an input vector to the linear-output ANN.

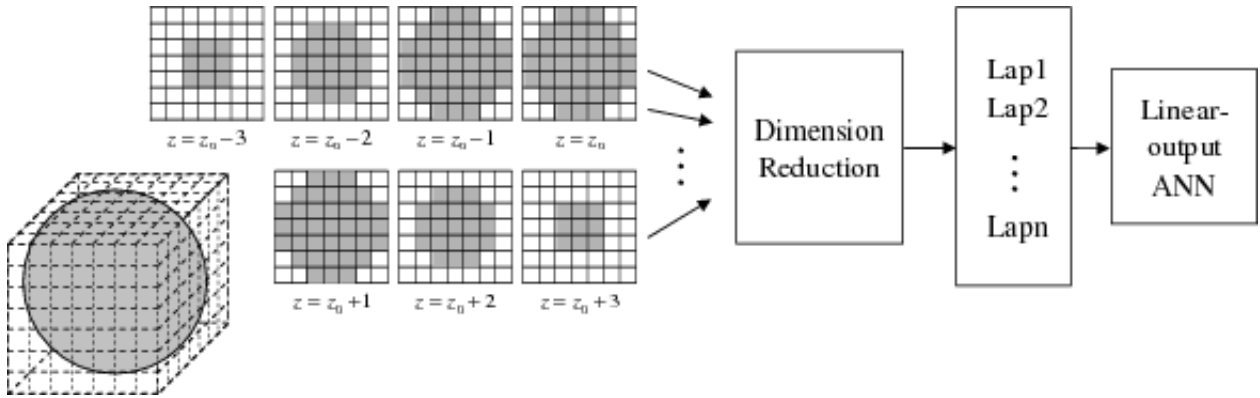


Figure 2: Dimensionality reduction of the scanning spherical input subvolume to the linear-output ANN via Laplacian eigenfunctons. Each square matrix represents a cross section at a certain z position in the input subvolume, where z_0 represents the central slice of the subvolume. A gray square in each section indicates the input voxel to the linear-output ANN, and a white square indicates an unused voxel. The 171 dimensional original input vector is converted to the LAPs vector. The top n LAPs are extracted and entered to the linear-output ANN.

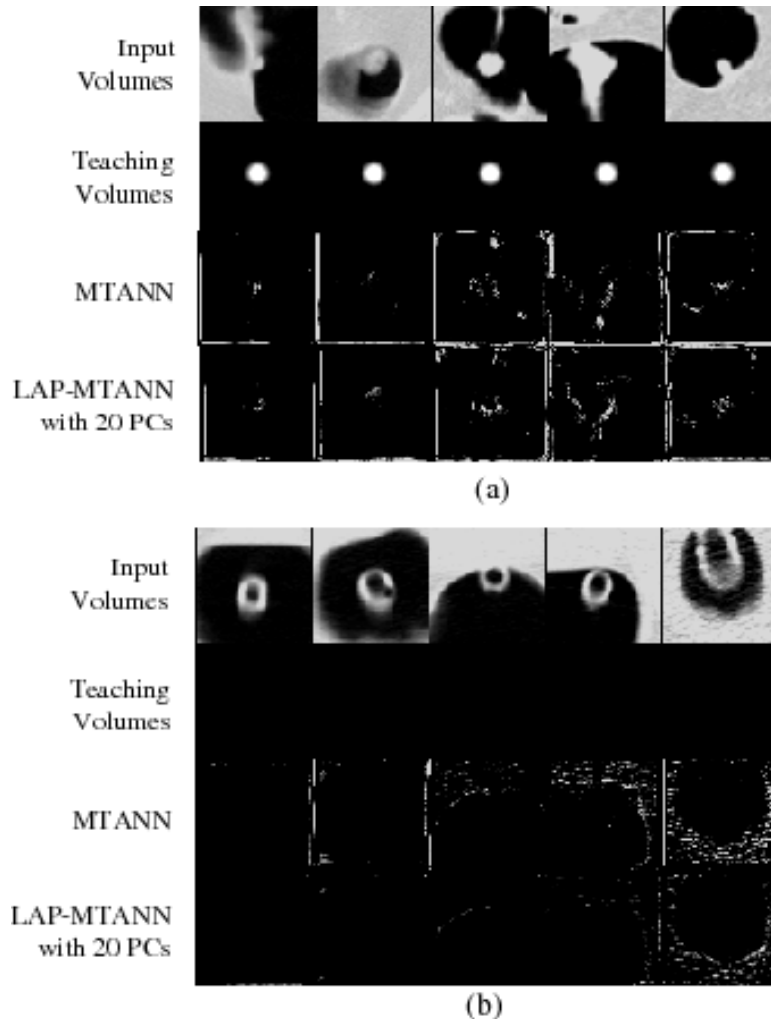


Figure 3: Illustrations of training (a) polyps and the corresponding output volumes of the trained original 3D MTANN and 3D LAP-MTANNs with top 20 eigenfunctions and (b) rectal tubes and the corresponding output volumes of the original 3D MTANN and 3D LAP-MTANNs in a resubstitution test. Shown are the central axial slices of 3D volumes. Teaching volumes for polyps contain 3D Gaussian distributions at the center, whereas those for non-polyps are completely dark, i.e., the voxel values for non-polyps are zero. In the output volumes of the original 3D MTANN and the 3D LAP-MTANNs, polyps are represented by bright voxels, whereas non-polyps are dark.

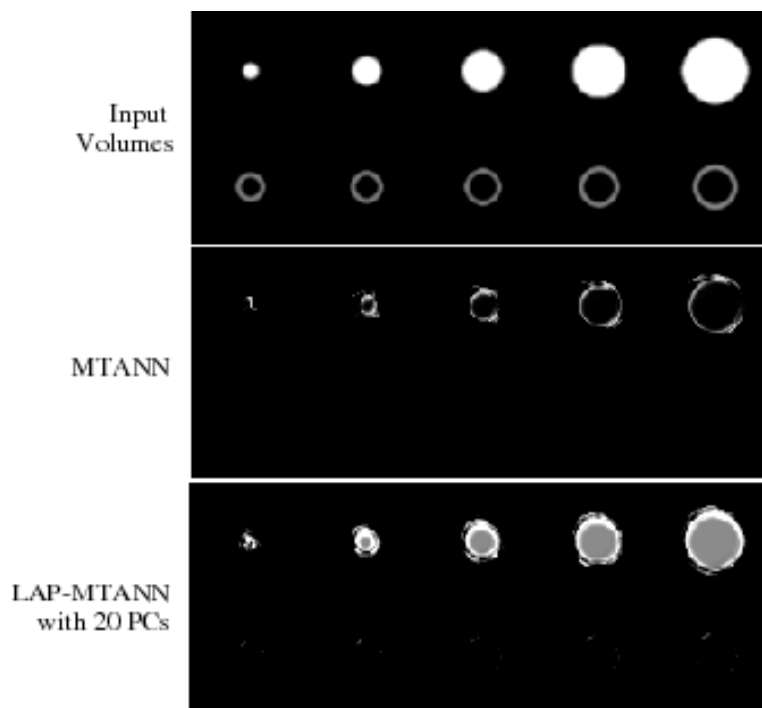


Figure 4: Illustrations of simulated polyps and rectal tubes and the corresponding output volumes of the original 3D MTANN and the LAP-MTANN with 20 eigenfunctions.

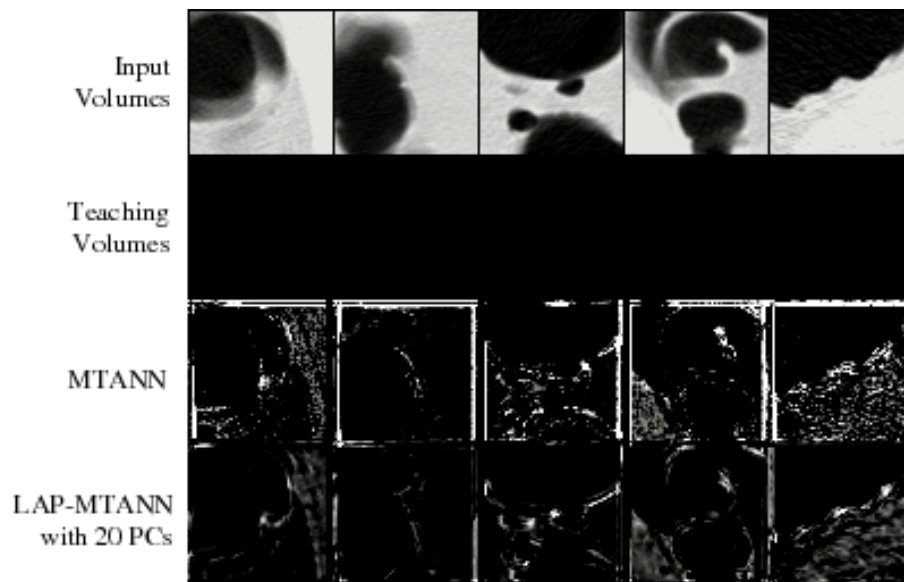


Figure 5: Illustrations of training non-polyps and the corresponding output volumes. The true polyps used for training are the same as for the simulation. The central axial slices of the 3D volumes are shown.

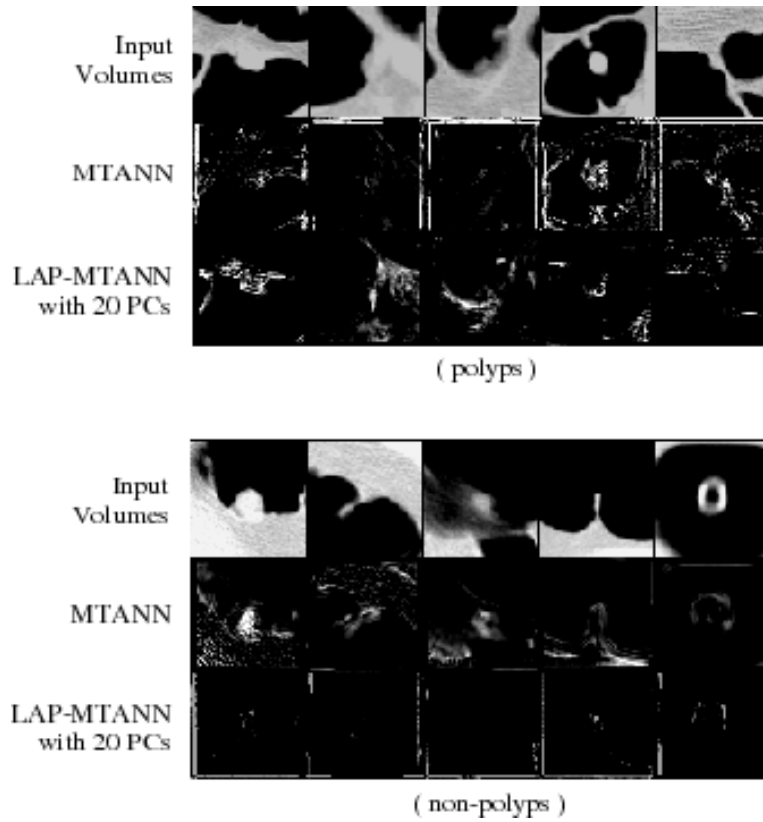


Figure 6: Illustrations of the performance of the trained 3D original and LAP-MTANNs with top 20 eigenfunctions on polyps and non-polyps, and the corresponding output volumes. The central axial slices of the 3D volumes are shown. The performance of the LAP-MTANN is comparable to that of the original MTANN.

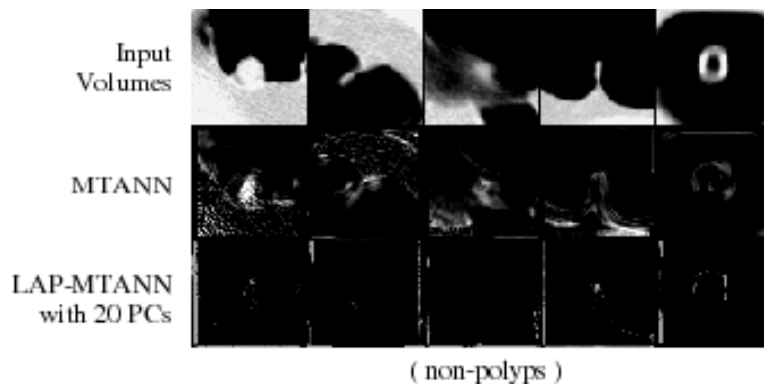


Figure 7: Illustrations of selected non-polyps, where the LAP-MTANN works better than the original MTANN on the first three and the original MTANN works better than the LAP-MTANN on the last two. The central axial slices of the 3D volumes are shown.

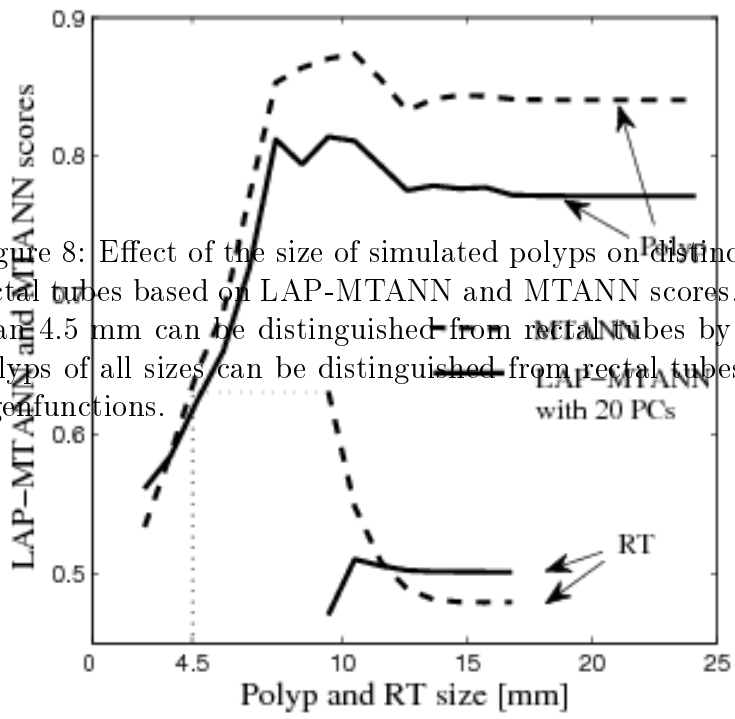


Figure 8: Effect of the size of simulated polyps on distinction between simulated polyps and rectal tubes based on LAP-MTANN and MTANN scores. Based on the scores, polyps larger than 4.5 mm can be distinguished from rectal tubes by the original 3D MTANN, whereas polyps of all sizes can be distinguished from rectal tubes by the 3D LAP-MTANN with 20 eigenfunctions.

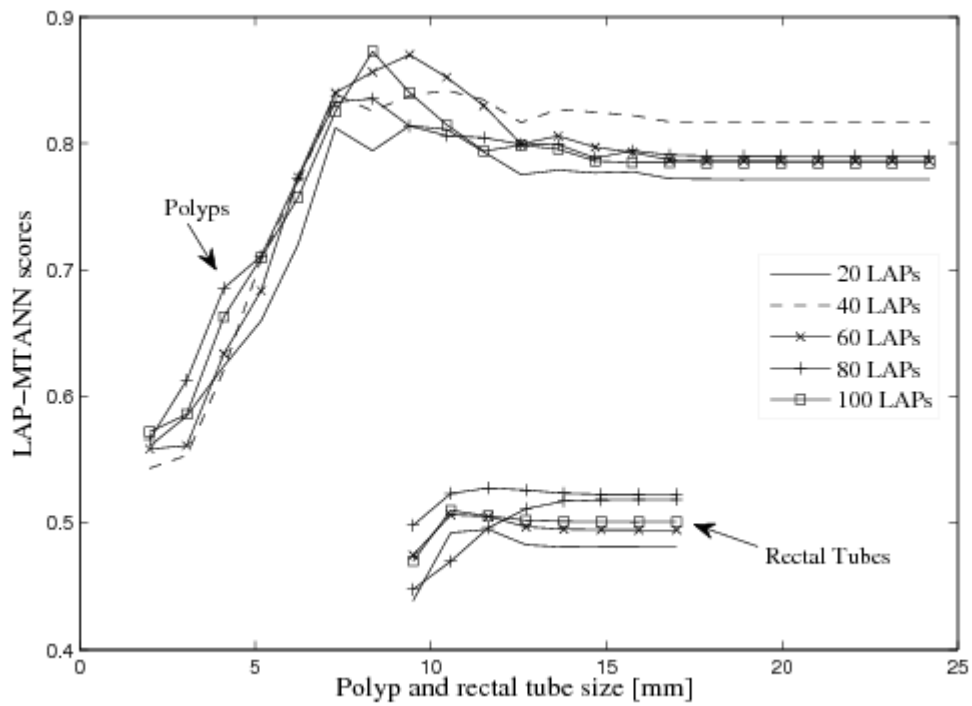


Figure 9: LAP-MTANN scores with various numbers of selected top Laplacian eigenfunctions in distinction between simulated polyps and rectal tubes.

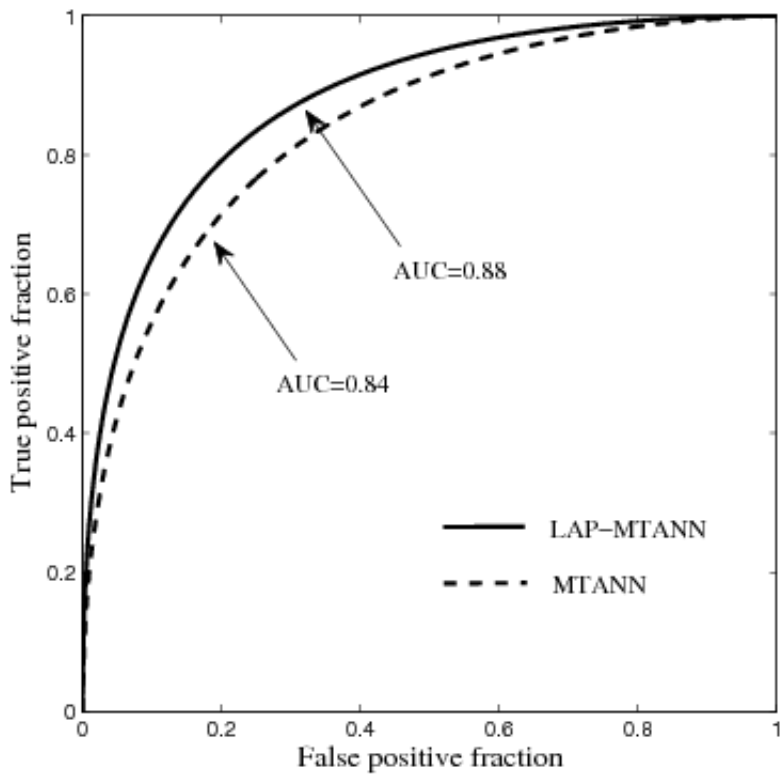


Figure 10: Comparison between the performance of the LAP-MTANN with 20 Laplacian eigenfunctions and that of the original MTANN. The difference between the AUC values for the ROC curves was not statistically significant ($p = 0.003$).

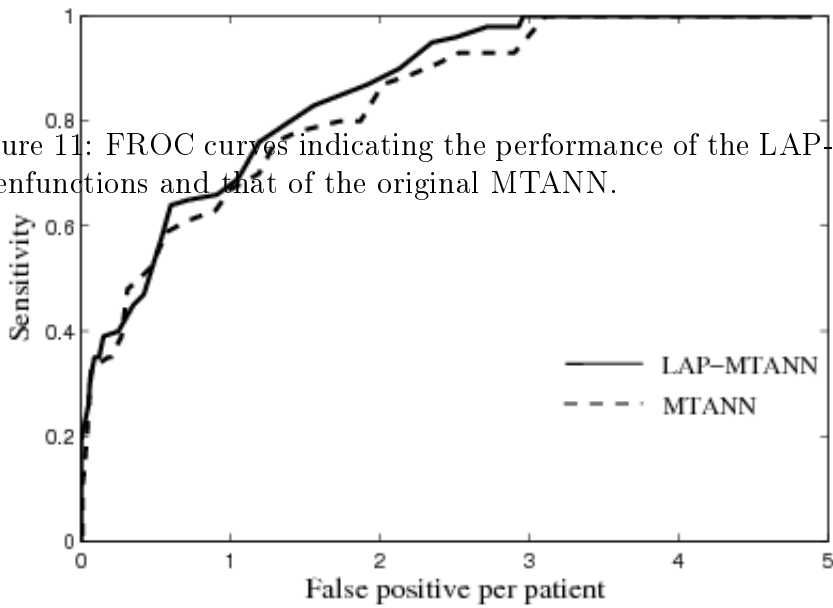


Figure 11: FROC curves indicating the performance of the LAP-MTANN with 20 Laplacian eigenfunctions and that of the original MTANN.

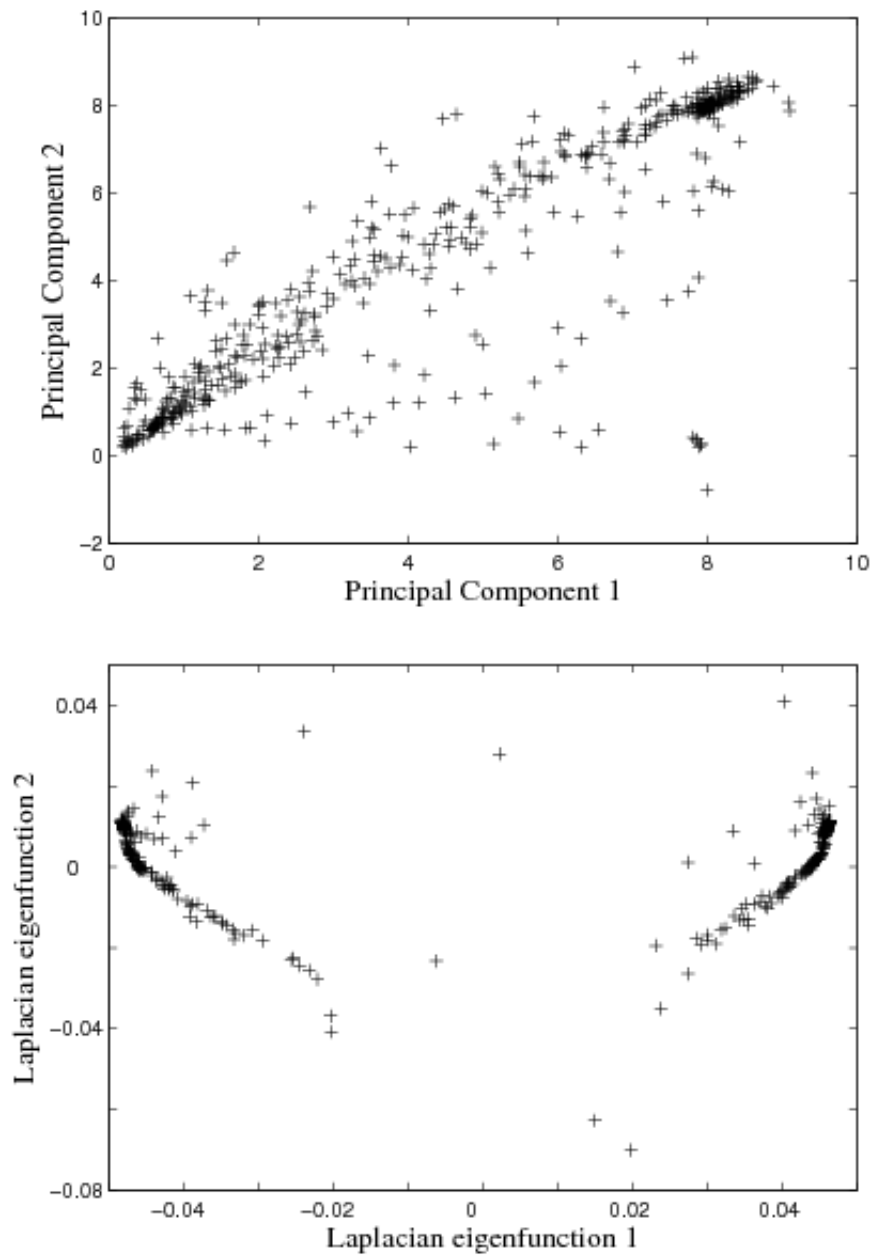


Figure 12: The top two PCs and Laplacian eigenfunctions of a set of 512 training patterns.

List of Tables

- I Comparisons of the performance (AUC values) of LAP-MTANNs with various numbers of top LAPs in distinction between actual polyps and non-polyps. AUC values, standard errors (SE) of AUC values and the p values for the AUC difference between each LAP-MTANN and the original MTANN are shown. . 33

Table I: Comparisons of the performance (AUC values) of LAP-MTANNs with various numbers of top LAPs in distinction between actual polyps and non-polyps. AUC values, standard errors (SE) of AUC values and the p values for the AUC difference between each LAP-MTANN and the original MTANN are shown.

	MTANN	LAP-MTANN										
		10	20	30	40	50	60	70	80	90	100	110
AUC	0.84	0.89	0.88	0.88	0.88	0.87	0.88	0.89	0.87	0.87	0.89	0.87
SE	0.03	0.03	0.03	0.03	0.03	0.03	0.03	0.03	0.03	0.03	0.03	0.03
p value	—	0.001	0.003	0.002	0.002	0.007	0.005	0.003	0.008	0.005	0.006	0.004